



Construction of Bi₂WO₆ homojunction via QDs self-decoration and its improved separation efficiency of charge carriers and photocatalytic ability

Chunmei Li^a, Gang Chen^{a,*}, Jingxue Sun^{a,*}, Hongjun Dong^{a,b}, Yu Wang^a, Chade Lv^a

^a Department of Chemistry, Harbin Institute of Technology, Harbin 150001, PR China

^b Department of Chemistry, Baicheng Normal University, Baicheng 137000, PR China

ARTICLE INFO

Article history:

Received 18 February 2014

Received in revised form 19 May 2014

Accepted 22 May 2014

Available online 2 June 2014

Keywords:

Homojunction

QDs self-decoration

Crystal growth mechanism

Charge separation behavior

Photodegradation mechanism

ABSTRACT

The Bi₂WO₆ homojunction is successfully synthesized via simple adjusting the amount of raw materials within a transitory hydrothermal reaction of 2 h. Such unique homojunction is constructed through the overgrowth of QDs on the nanoflake unit surfaces of the Bi₂WO₆ hierarchical structure, which alters the optical absorption property of the samples owing to quantum effect. Photocurrent responses and PL spectra indicate Bi₂WO₆ homojunction can effectively separate electron-hole pairs and suppress their recombination. The as-prepared samples show the higher efficiency for the photocatalytic degradation of the typical RhB dye compared with the previous reported hierarchical structured Bi₂WO₆ under visible light. This work provides a new strategy for improving photodegradation activity of Bi₂WO₆ photocatalyst.

© 2014 Elsevier B.V. All rights reserved.

1. Introduction

Environmental problems associated with harmful organic pollutants in water have become an arduous challenge to the sustainable development of modern human society. In recent years, photocatalysts as a kind of “green” energy have attracted substantial interest for water splitting and degradation of organic contaminants under UV or visible-light [1–5]. As is well known, the photocatalytic reaction is usually regarded as the photon direct absorption by the energy band gap of semiconductor materials [6,7]. Upon photo-excitation, the electron–hole pairs can separate and transfer to the semiconductor surface where photocatalytic reactions take place [8,9]. Heretofore, the efficient charge separation plays a key role for improving photocatalytic activity and determining the conversion efficiency of solar energy.

The surface decoration of photocatalysts is one of the developed effective methods to facilitate interfacial charge transfer and separation [10,11]. In particular, the photocatalyst decorated with quantum dots (QDs) exhibits the better photocatalytic performance because QDs may employ hot electrons or generate multiple charge carriers with a single photon to enhance

light-energy conversion efficiency as well as effectively decrease the recombination of charge carriers [12,13]. In addition, constructing homojunction is considered to be an effective way for improving transferred and separated efficiency of charge carriers recently [14,15]. Especially, the homojunction formed by QDs self-decorated TiO₂ nanosheet was prepared by multi-step high temperature calcination, which presents improved photocatalytic activity [16]. But the wide band gap (3.2 eV) of TiO₂ limits its practical application. Furthermore, Bi₂WO₆ as a promising photocatalyst has been proved to possess admirable photocatalytic oxygen liberation from water and organic pollutant decomposition under visible light [17–21]. Therefore, the modification of Bi₂WO₆ is an important and imperative to further improve photocatalytic ability. In previous reports, most modifications of Bi₂WO₆ are achieved via forming heterojunction with employing noble metal, such as Ag/Bi₂WO₆ [22], AgBr/Ag/Bi₂WO₆ [23], Ag₂O/Bi₂WO₆ [24], Au/Bi₂WO₆ [25], Pt/Bi₂WO₆ [26], PtCl₄/Bi₂WO₆ [27], Pd/Bi₂WO₆ [28] and so on. In contrast with the above heterojunctions, the constructing Bi₂WO₆ homojunction via the surface QDs self-decoration method is rarely reported and may be a more effective alternative.

At present work, the Bi₂WO₆ homojunction is constructed by virtue of QDs *in-situ* germinating on the nanoflake unit surfaces of the hierarchical structure, which presents the obvious improved photocatalytic ability compared with the previous reported hierarchical structured Bi₂WO₆. The synthesis of homojunction is achieved by only increasing 5% sodium tungstate raw materials

* Corresponding author. Tel.: +86 451 86413753; fax: +86 451 86413753.

E-mail addresses: gchen@hit.edu.cn (G. Chen), jxsun@hit.edu.cn (J. Sun).

and using a transitory hydrothermal reaction of 2 h, the facility, cheapness and non-pollution of which are desired in practical application. The possible crystal growth mechanism, transfer and separation behavior of charge carriers and photocatalytic mechanism are expounded in depth.

2. Experimental

2.1. Preparation and characterizations

All the raw materials were purchased from commercial sources and used without further purification. In a typical synthesis, sodium tungstate ($\text{Na}_2\text{WO}_4 \cdot 2\text{H}_2\text{O}$) was added into the bismuth nitrate ($\text{Bi}(\text{NO}_3)_3 \cdot 5\text{H}_2\text{O}$) solution drop by drop under vigorous magnetic stirring for 1 h, and then the suspension was transferred into a 25 mL Teflon lined stainless steel autoclave to carry out hydrothermal process at 160°C . After cooling down to room temperature, the solid sample was collected by centrifugation and washed with deionized water and ethanol in turn. Bi_2WO_6 product was finally obtained by drying at 80°C for 20 h. Using the stoichiometric ratio (W: Bi = 0.5), the typical hierarchical structured Bi_2WO_6 (B0) was prepared by 20 h hydrothermal reaction. When the W/Bi ratio was adjusted to 0.525 (5% excess of W source, B5), the QDs self-decorated Bi_2WO_6 with hierarchical structure was prepared by only 2 h hydrothermal reaction (B5-2h). Further prolonging reaction time to 20 h, the hierarchical structured Bi_2WO_6 decorated with more QDs was obtained (B5-20h).

The phase of the as-prepared Bi_2WO_6 samples was characterized by powder X-ray diffractometer (XRD, RigakuD/max-2000) equipped with a Cu-K α radiation at a scanning rate of 5°min^{-1} in the 2θ range of $10\text{--}90^\circ$. X-ray tube current and voltage were set at 50 mA and 45 kV, respectively. X-ray photoelectron spectroscopy (XPS) analysis was measured on an American electronics physical HI5700ESCA system with X-ray photoelectron spectroscopy using Al K α (1486.6 eV) monochromatic X-ray radiation. The peak positions were corrected against the C 1s peak (284.6 eV) of contaminated carbon. The morphologies of the samples were characterized by field-emission scanning electron microscopy (FESEM, FEI QUANTA 200F). Transmission electron microscopy (TEM) and high-resolution TEM (HR-TEM) of the samples were carried out on FEI Tecnai G2 S-Twin operating at 300 kV. The UV–vis diffuse reflectance spectra (DRS) of the samples were recorded on a UV–vis spectrophotometer (PG, TU-1900) with BaSO_4 as the background between 200 nm and 900 nm at room temperature. Raman spectra were recorded on a Renishaw via micro-Raman spectroscopy system in the backscattering geometry with a 458 nm argon-ion laser as the excitation source. The nitrogen adsorption and desorption isotherm, pore size distribution and specific surface area were measured at 77 K using an AUTOSORB-1 Surface Area and Pore Size Analyzer. The photoluminescence (PL) spectra were measured by the Perkin Elmer LS55 at room temperature.

2.2. Photocatalytic and photoelectrochemical measurements

The photocatalytic activities were determined by the degradation of RhB and phenol aqueous solution under visible light irradiation in quartz photochemical reactor. A 300 W Xenon lamp (Trusttech PLS-SXE 300, Beijing) covered with a UV filter ($\lambda > 400 \text{ nm}$) was used as a light source. The photodegradation was performed at room temperature as follows: the RhB solution (10 mg L^{-1} , 100 mL) containing 0.05 g Bi_2WO_6 was carried out after 5 min of ultrasonic process and kept in dark for 1 h to achieve adsorption–desorption equilibrium between dyes and photocatalysts under continuous magnetic stirring before irradiation. Every 10 min of time intervals, 3 mL mixture was collected

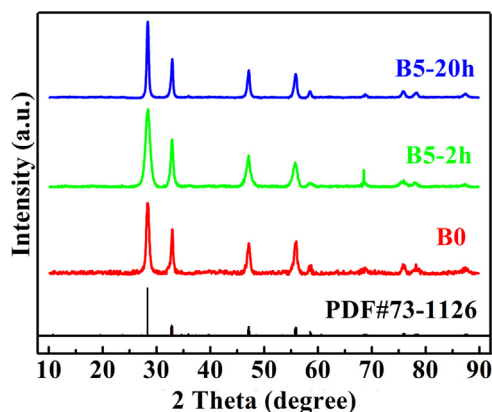


Fig. 1. XRD patterns of B0, B5-2h and B5-20h samples.

from the suspension, followed by centrifuged at 10^4 rpm for 3 min. The absorbance of RhB solution was analyzed by measuring the absorbance at $\lambda = 554 \text{ nm}$ with the UV–vis spectrophotometer (PG, TU-1900). Moreover, the photodegradation of phenol was similar to that of RhB solution. The phenol solution (20 mg L^{-1} , 100 mL) containing 0.05 g Bi_2WO_6 sample was magnetic stirred for 1 h in the dark, then adding 0.2 mL H_2O_2 to reactor before irradiation. 3 mL mixture was collected and centrifuged from the suspension every 1 h. The absorbance of phenol solution was analyzed by measuring absorbance at $\lambda = 270 \text{ nm}$.

The photoelectrochemical characteristics were measured in a CHI604C electrochemical working station using a standard three-compartment cell under visible light provided by a 300 W Xe lamp. The Bi_2WO_6 sample coated at FTO glass, a piece of Pt sheet, a Ag/AgCl electrode and 0.01 M sodium carbonate were used as the working electrode, the counter-electrode, the reference electrode and the electrolyte, respectively.

3. Results and discussion

The composition of homojunction is identified by XRD. Fig. 1 shows that the XRD of all the as-prepared samples with the similar diffraction patterns can be well-indexed as orthorhombic Bi_2WO_6 (JCPDS card No. 73-1126), which implies the identical crystalline phase products of B0, B5-2h and B5-20h are obtained. The sharp and intense diffraction peaks indicate that the as-prepared samples have high-crystallinity. The morphologies of Bi_2WO_6 samples are confirmed by FESEM. As shown in Fig. 2a–c, the FESEM images of B0, B5-2h and B5-20h exhibit largescale monodispersed flower-like microspheres with diameter of 2–4 μm . In addition, the EDS spectra of Bi_2WO_6 samples in Fig. 2d exhibit that the samples contain Bi, O and W elements and all the atomic ratios of Bi to W to O are close to 2:1:6, which demonstrate the excess amount of W source has no influence on sample compositions. The detailed morphology characteristics are investigated by TEM. Fig. 3a–c show the TEM images of the individual microsphere samples, where all the B0, B5-2h and B5-20h samples present hierarchical architecture characteristics built by self-assembly of the two-dimensional nanoflakes. The aggregation of the nanoflakes results in generating numerous hierarchical pores on nanoscale, which may enhance the physicochemical properties and act as transport paths for small molecules [18]. The SAED patterns of the individual microsphere for B0, B5-2h and B5-20h in the insets of Fig. 3a–c exhibit an obvious diffraction ring, respectively. This result reveals that the integrated assembly of Bi_2WO_6 samples have a polycrystalline inherent quality, indicating the flower-like microsphere is composed of the nano-crystalline subunits. The high-magnification TEM images of the individual nanoflake units for B0, B5-2h and B5-20h samples are performed. It

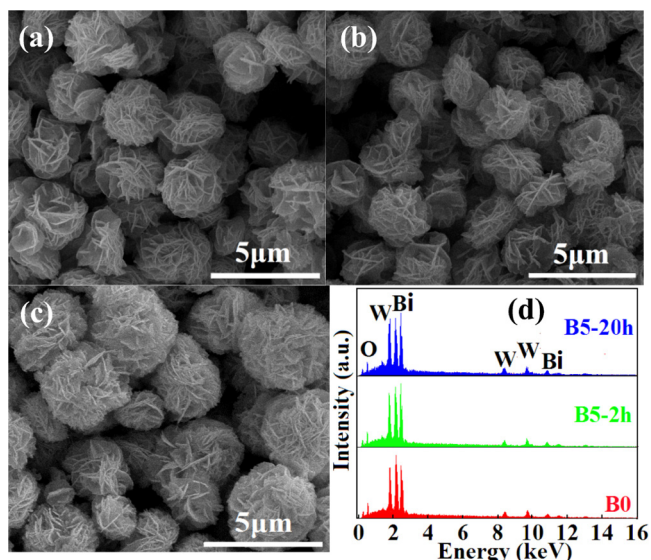


Fig. 2. FESEM images of B0 (a), B5-2h (b) and B5-20h (c) samples and the corresponding EDS spectra (d).

is noteworthy that the nanoflake unit of B0 presents a smooth surface in Fig. 3d. The interplanar spacing d value is 0.315 nm on the HR-TEM images in Fig. 3g, which corresponds to the (1 1 3) planes of orthorhombic Bi_2WO_6 [29]. Interestingly, many uniformly distributed QDs with the diameter in the range of 5–10 nm are clearly observed on the nanoflake unit surfaces of B5-2h and B5-20h in Fig. 3e and f. Importantly, the Bi_2WO_6 QDs are crystalline as can be perceived from the oriented lattice fringes constituting the dots [30]. The HR-TEM images (Fig. 3h and i) present that the lattice fringe directions of QDs and nanoflake are obviously different. The

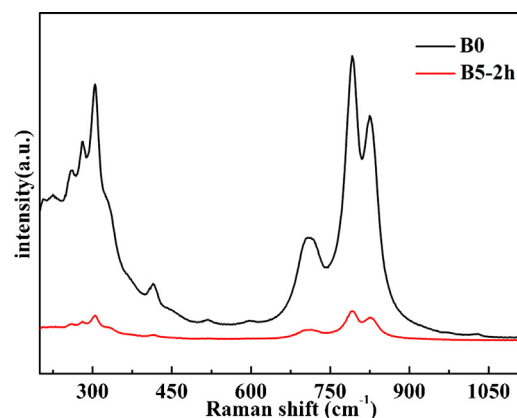


Fig. 4. Raman spectra of B0 and B5-2h.

interplanar spacing d values of the QDs and nanoflake are both 0.315 nm, which agree well with the (1 1 3) planes of Bi_2WO_6 identically. Additionally, the Raman spectra (Fig. 4) are further tested to verify the formation of Bi_2WO_6 QDs on the nanoflake surface. The Raman intensity reduces relatively as the particle size decrease [31]. The Raman intensity of B5-2h is weaker distinctly than that of B0, which may result from size effect of surface QDs, further evidencing QDs generation on the nanoflake unit surfaces. All the above demonstrate that the Bi_2WO_6 homojunction is constructed by QDs germinating *in-situ* on the nanoflake unit surfaces of hierarchical structure.

Furthermore, the crystal growth mechanism of homojunction constructed by self-decoration of Bi_2WO_6 QDs on the nanoflake unit surfaces of hierarchical structure is investigated. The FESEM images and XRD patterns of samples at different time intervals in Fig. S1 (Supporting information) suggest that it belongs to an

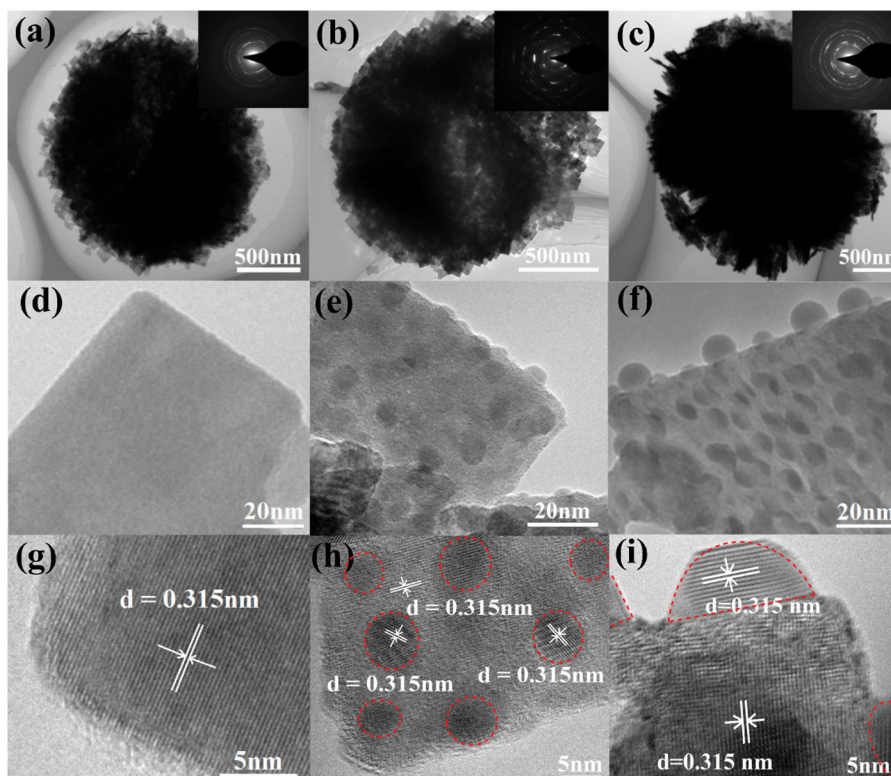


Fig. 3. TEM images of B0 (a and d), B5-2h (b and e) and B5-20h (c and f), the corresponding SAED (the insets of (a)–(c)) of the individual microsphere as well as HR-TEM images ((g)–(i)) of the individual nanoflake units and QDs.

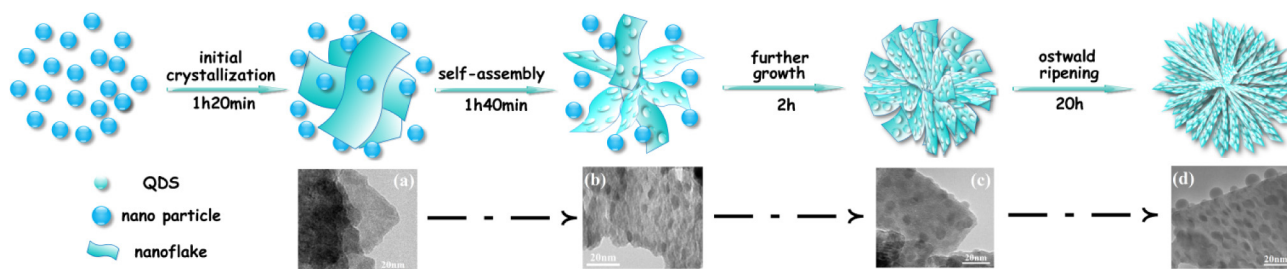


Fig. 5. The schematic diagram of crystal growth mechanism for the QDs self-decorated Bi_2WO_6 homojunction.

obvious self-assembly and Ostwald ripening mechanism [32,33]. From the FESEM in Fig. S1a and XRD pattern of B5-1h in Fig. S1e, Bi_2WO_6 nanoparticles with low crystallinity are formed after 1 h hydrothermal reaction. With increasing the reaction time to 1 h and 20 min, the FESEM image in Fig. S1b displays that the irregularity Bi_2WO_6 nanoflake units generate via an “initial crystallization” process based on Gibbs–Thomson law [34,35]. In this process, the irregularity nanoflake surfaces are smooth (TEM image a in Fig. 5). The interlayered Bi_2WO_6 nanoflakes appear owing to the “self-assembly” process after a reaction time of 1 h and 40 min on the FESEM image in Fig. S1c and the crystallinity of the samples are improved from the narrowing XRD pattern of B5-1h 40 min in Fig. S1e. A small amount of Bi_2WO_6 QDs are formed by the *in situ* growth on the nanoflake unit surfaces in this process (TEM image b in Fig. 5). When the reaction time reaches to 2 h, the flower-like hierarchical structured Bi_2WO_6 with high crystallinity are formed according to the FESEM image in Fig. S1d and XRD pattern of B5-2h in Fig. S1e. Meanwhile, more QDs appear on the nanoflake surfaces (TEM image c in Fig. 5). Further prolonging the reaction time to 20 h, the Bi_2WO_6 hierarchical structure is more integrity by Ostwald ripening process and the whole nanoflake surfaces are almost covered with QDs (TEM image d in Fig. 5).

Based on the above analysis, as a comparison with the smooth nanoflake surfaces of B0 (Fig. 3d), we can infer that excess W raw material is the dominant factor for generating and growing of Bi_2WO_6 QDs with the formation of flower-like hierarchical structure. The construction of QDs self-decorated Bi_2WO_6 homojunction can be a typical kinetic overgrowth process. In the process of the kinetic growth, the diffusion rate (V_1) of a precursor to the surface and the growth rate (V_2) at which the atoms generated and added on the surface active sites have much effect on the crystal growth action [36,37]. When V_1 is larger than V_2 , the diffusion can be fast enough to keep the concentrations of the precursor equal in close to the surface active sites. The atoms have identical possibility to add on different active sites, so no prior overgrowth emerges under such circumstances. But on the contrary (V_1 is smaller than V_2), the atoms add on the active sites with a rapid decrease in concentration for approximate the surface active sites [38]. Due to the existence of excess W source, Bi source is insufficient during this reaction. When Bi_2WO_6 nanoflake is formed, the excess W source can be absorbed on the surface active sites. Then the Bi source in close proximity to the surface active sites reacts fleetly with W source absorbed on the surface active sites of Bi_2WO_6 nanoflakes. So QDs self-decorated Bi_2WO_6 homojunction is obtained with preferential overgrowth on the nanoflake surfaces. The overgrowth phenomenon usually takes place in the bicomponent heterojunction formation with one excessive component in the precursor [39–41]. To our knowledge, the construction of homojunction with hierarchical structure via the “over growth” process is achieved barely in the literatures. The schematic diagram of crystal growth mechanism for the QDs self-decorated Bi_2WO_6 with hierarchical structure is illustrated in Fig. 5.

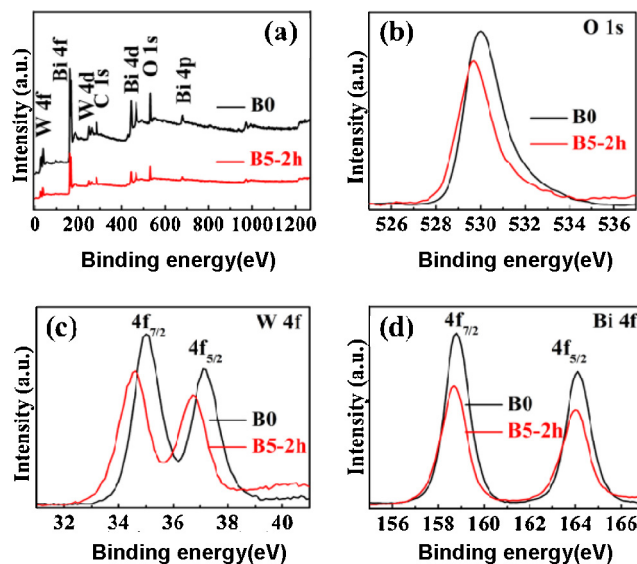


Fig. 6. Survey (a) and high-resolution XPS spectra of O 1s (b), W 4f (c) and Bi 4f (d) for B0 and B5-2h samples.

We all know that the QDs with certain size can cause quantum-size effect considering the homologous physicochemical properties of original nanostructure for the samples [42–44], which is certified by variation of binding energy of XPS spectra [45]. The survey XPS spectra of B0 and B5-2h samples are shown in Fig. 6a, where the different binding energy are assigned to W 4f, Bi 4f, W 4d, C 1s, O 1s, Bi 4p states and O auger peaks. The high-resolution XPS spectra of the B0 and B5-2h samples are further measured. The binding energy peaks at 530.0 eV, 158.8 and 164.1 eV as well as 35.0 and 37.1 eV of the B0 samples in Fig. 6b–d belong to O 1s, W 4f_{7/2} and W 4f_{5/2} as well as Bi 4f_{7/2} and W 4f_{5/2} states, respectively. It is noticed that the binding energies of O 1s, W 4f and Bi 4f of B5-2h remarkably shift about 0.3, 0.4 and 0.1 eV to the lower binding energy compared with that of B0, which demonstrates the existence of quantum confinement effects and interaction between QDs and nanoflake units of Bi_2WO_6 [46].

Meanwhile, the quantum confinement effect can also alter the optical absorbance property [47,48]. The UV–vis DRS of B0, B5-2h (Fig. 7) and B5-20h (Fig. S2) samples exhibit the obviously visible harvest ability. The absorbance edges of B5-2h and B5-20h take place blue shift owing to QDs size effect, and their steep shape indicate that the optical absorption is due to the band-gap transition rather than the impurity level [49]. The plots of $(\alpha h\nu)^{1/2}$ versus $h\nu$ for B0 and B5-2h samples in the inset of Fig. 7 show that the band gap value varies from 2.75 eV of B0 to 2.84 eV of B5-2h. The absorbance edge blue shift and widened band gap may be attributed to confinement effect of the surface QDs caused by forming discrete energy levels in the semiconductor [50], which implies that Bi_2WO_6

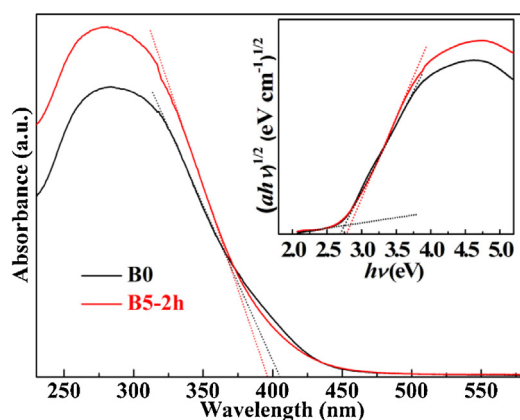


Fig. 7. UV-vis DRS and plots of $(\alpha h\nu)^{1/2}$ versus $h\nu$ (the inset) of B0 and B5-2h samples. (For interpretation of the references to color in this figure legend, the reader is referred to the web version of this article.)

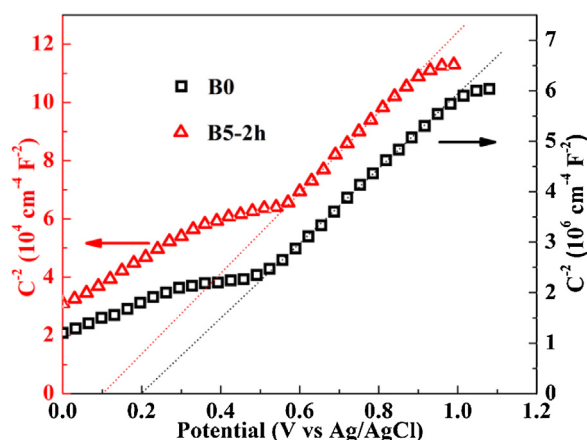


Fig. 8. Mott-Schottky plots of B0 and B5-2h samples as an electrode.

homojunction is constructed between QDs and nanoflake units in B5-2h samples.

As revealed from UV-vis DRS in Fig. 7, Bi_2WO_6 QDs decorated on the nanoflake units result in the enlarged band gap. In order to further explore the construction of homojunction, the values of the relative conduction band (CB) and valence band (VB) position for B0 and B5-2h samples are calculated in Table S1 (Supporting information). The CB and VB values of B5-2h shift up ~ 0.04 eV and move down ~ 0.05 eV in comparison with that of B0, which attribute to the quantum effect of Bi_2WO_6 QDs on the nanoflake unit surfaces and provide essential thermodynamic requirements for the transfer of electrons and holes. Furthermore, the shifting up of CB for B5-2h is verified by the investigation of flat-band potential. Fig. 8 shows the Mott-Schottky plots of the B0 and B5-2h films as an electrode, respectively, the positive slope of which in the linear region indicates they are in accordance with n-type semiconductor characteristic. It is found that the flat-band potential position of B5-2h (0.11 V) is 0.07 V higher than that of B0 (0.18 V) under the same experimental condition. The CB potentials of n-type semiconductors are very close to (0.1–0.2 eV more negative) the flat-band potentials [51]. We can further deduce that the CB position of B5-2h is more negative than that of B0. Therefore, Bi_2WO_6 homojunction is constructed by QDs self-decoration on the nanoflake unit surfaces of hierarchical structure owing to the different CB and VB positions of QDs and nanoflakes, thus resulting in improved separation efficiency of charge carriers.

The photocatalytic activity of different photocatalysts is appraised by degradation of the typical RhB dye under visible light.

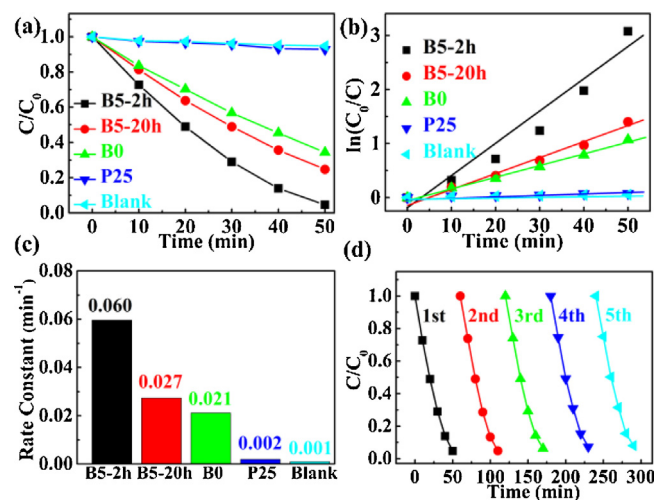


Fig. 9. Dynamic curves of photodegradation (a), plots of $\ln(C_0/C)$ versus time (b) and rate constant k (c) for RhB solutions over different samples under visible light; cycling photodegradation runs (d) for RhB solutions over B5-2h samples under visible light.

From the dynamic curves of RhB degradation in Fig. 9a, it is found that all the Bi_2WO_6 samples display more intense photodegraded activity than Degussa P25 (TiO_2). We notice that the photocatalytic activities of B5-2h and B5-20h samples are obviously higher than that of B0. In particular, B5-2h sample presents the most outstanding photodegradation ability and completely decomposes RhB within 50 min. In addition, the degradations of RhB over the B5 samples achieved at different reaction time are performed. As shown in Fig. S3 (Supporting information), with prolonging hydrothermal reaction time, the photodegradation ability of B5 samples reduces, which possibly arises from the generated excessive QDs acting as recombination centers of charge carriers. Moreover, the kinetic curves of RhB degradation can be approximated as a pseudo-first-order process [52]. The plots of $\ln(C_0/C)$ versus irradiation time are shown in Fig. 9b. Using the fitting results of these plots, we achieve that the removal rate constant k of RhB over B5-2h are 0.060 min^{-1} , which amazingly reaches about 2.22, 2.86 and 30 times as much as that of B5-20h (0.027 min^{-1}), B0 (0.021 min^{-1}) and P25 (0.002 min^{-1}) in Fig. 9c, respectively. Furthermore, in order to assess the reusability and stability of the photocatalysts which are crucial for practical application, the cycle experiments of RhB degradation are performed. The photocatalytic ability of B5-2h has not significantly loss after five recycles (Fig. 9d), indicating that the as-prepared sample possesses ideal stability and durability.

In addition, in order to assess photocatalytic reaction pattern, the photodegradation experiment of RhB over B5-2h sample with monochromatic central wavelength irradiation is performed [3]. As shown in Fig. S4, the monochromatic central wavelength with 550 nm visible light is applied to excite RhB molecules instead of B5-2h sample. The result displays that RhB are only decomposed less than 5% after 50 min and lower than that of B5-2h sample under visible light ($\lambda > 400 \text{ nm}$), which proves that the effect of photosensitization of RhB over B5-2h sample during degradation processes is negligible. Hence, we can confirm that the self-oxidation behavior instead of the effect of photosensitization brings about the RhB degradation over B5-2h sample. Moreover, for further verifying the self-oxidation ability of B5-2h sample, the photodegradation of phenol (test molecule of non-absorbing visible light) solution is carried out. It is observed from Fig. S5 the phenol solution is almost completely decomposed after 5 h under visible light. All

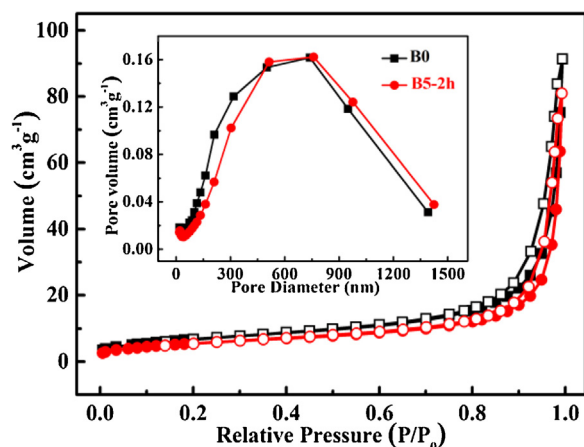


Fig. 10. N_2 adsorption–desorption curves and pore diameter distributions (inset) of B0 (black) and B5-2h (red) samples. (For interpretation of the references to color in this figure legend, the reader is referred to the web version of this article.)

above demonstrate that B5-2h sample is a kind of outstanding photocatalyst.

For investigating the influence of pore diameter distribution and BET surface area on the resulting enhanced photocatalytic ability, the N_2 adsorption–desorption experiments are carried out. As shown in Fig. 10 and Fig. S6, B0, B5-2h and B5-20h samples show the similar adsorption–desorption characteristic and pore diameter distribution (the insets of Fig. 10 and Fig. S6). In addition, the BET surface areas of B5-2h ($20.48 \text{ m}^2 \text{ g}^{-1}$) and B5-20h ($19.66 \text{ m}^2 \text{ g}^{-1}$) are less than that of B0 ($25.02 \text{ m}^2 \text{ g}^{-1}$). Therefore, the effects of these factors on improved photocatalytic ability of B5-2h and B5-20h samples are insignificant and neglectful. As a result, it further indirectly attests the enhanced photocatalytic activity ascribes the construction of homojunction that improves the transferred and separated efficiency of charge carriers.

Actually, the large magnitude of photocurrent suggests the high charge collection efficiency of the electrode surface, and indirectly demonstrates the high separated efficiency of electron-hole pairs [53,54]. Fig. 11 demonstrates that the B0 and B5-2h films as photoelectrodes are quickly generating photocurrent under visible light. It is noticed that B5-2h sample produces the more intense photocurrent in comparison with B0, which indicates that the separated efficiency and the lifetime of the photogenerated charge carriers are improved as a result of the formation of Bi_2WO_6 homojunction. The result is further evidenced by the photoluminescent (PL) spectra, because it is usually served as an effective approach to explore the recombination rate of charge carriers [55–57]. The PL spectra of B0 and B5-2h in the inset of Fig. 11 show a strongly wide emission peak at $\sim 396 \text{ nm}$, which corresponds to band gap

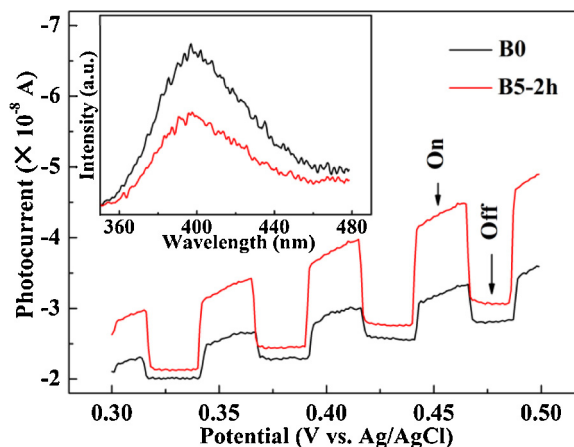


Fig. 11. Photocurrent responses and PL spectra (inset) of B0 and B5-2h samples.

transition. Interestingly, an obvious fluorescence quenching takes place in the PL spectra of B5-2h. This suggests that QDs germinating on the Bi_2WO_6 nanoflake unit surfaces efficiently separate photogenerated electron-hole pairs and reduce their recombination rate.

Fig. 12 provides the relative band position schematic between QDs and nanoflake units of hierarchical structure as well as possibly transferred and separated behavior of charge carriers and photocatalytic reaction mechanism over the QDs self-decorated Bi_2WO_6 homojunction. Both the QDs and nanoflake units composing of Bi_2WO_6 homojunction generate electron-hole pairs under visible light. Then the electrons and holes on the CB and VB of Bi_2WO_6 QDs immediately transfer to that of Bi_2WO_6 nanoflakes due to their different positions, respectively. Meanwhile, because the effective mass of the electrons is much larger than that of holes, the longer time required for electrons to migrate to the same destination in the same crystals than that for holes [58]. In this process, the transfer velocity of holes is faster than that of electrons, which leads to more electrons and holes assembling on the CB of QDs and VB of nanoflakes, respectively, thus improving the separated efficiency of the photogenerated charge carriers. To further clarify the contributions of electrons and holes, $\text{Fe}(\text{NO}_3)_3$ (electron scavenger) and EDTA-2Na (hole scavenger) are used for exploring the main reactive species in the photocatalytic degradation process of RhB (Fig. S7). The trapping experiments show that the addition of the hole scavenger (EDTA-2Na) only causes a small decrease of photocatalytic activity of B5-2h. In contrast, when the electron scavenger ($\text{Fe}(\text{NO}_3)_3$) is added to the photocatalytic reaction system, the photocatalytic activity is seriously suppressed. These results reveal that the superoxide radical $\bullet\text{O}_2^-$ play the major roles in

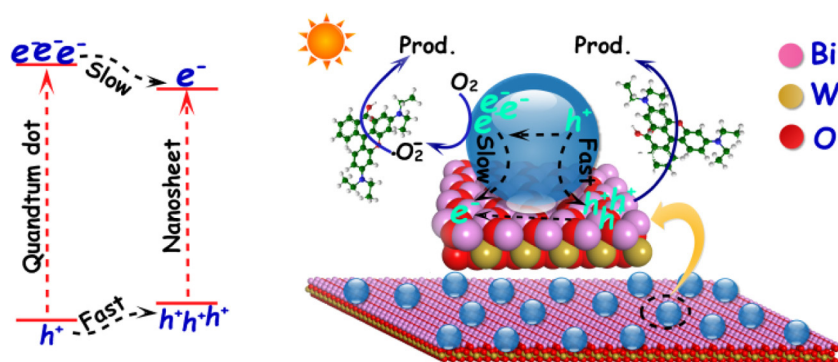


Fig. 12. Relative band position schematic between QDs and nanoflakes as well as possibly transferred and separated behavior of charge carriers and photocatalytic reaction mechanism over B5-2h.

the typical RhB photodegradation process, which coincides with the previous reports [59]. Under the visible light irradiation, the abundance of photogenerated electrons and holes assemble on QDs and nanoflakes of Bi_2WO_6 . The electrons can be captured by O_2 in the solution to produce oxidative activated species $\bullet\text{O}_2^-$, further decomposing RhB molecules. In addition, the photogenerated holes can also directly degrade RhB molecules.

4. Conclusion

The Bi_2WO_6 homojunction is successfully constructed by virtue of QDs self-decoration method through only increasing 5% sodium tungstate raw materials and using a simple, eco-friendly and transitory hydrothermal reaction. Bi_2WO_6 QDs germinating *in-situ* on the nanoflake unit surfaces of the hierarchical structure exhibits obviously quantum effect, which alter the optical absorbance property and energy band position. It gives rise to the formation of Bi_2WO_6 homojunction that effectively separates electron-hole pairs thus remarkably improves photocatalytic ability. The achieved homojunction via QDs self-decoration as a result of the typical “over growth” phenomenon provides a new strategy for improving photodegradation activity of Bi_2WO_6 photocatalyst.

Acknowledgments

This work was financially supported by the National Natural Science Foundation of China (21071036 and 21271055) and Province Natural Science Foundation of Heilongjiang Province (ZD201011). We acknowledge for the support by Open Project of State Key Laboratory of Urban Water Resource and Environment, Harbin Institute of Technology (No. QAK201304) and Program for Innovation Research of Science in Harbin Institute of Technology (PIRS of HIT B201412).

Appendix A. Supplementary data

Supplementary data associated with this article can be found, in the online version, at <http://dx.doi.org/10.1016/j.apcatb.2014.05.041>.

References

- [1] M. Wu, X. Lin, Y. Wang, L. Wang, W. Guo, D. Qi, X. Peng, A. Hagfeldt, M. Grätzel, T. Ma, J. Am. Chem. Soc. 134 (2012) 3419–3428.
- [2] Y.H. Lv, Y.Y. Zhu, Y.F. Zhu, J. Phys. Chem. C 117 (2013) 18520–18528.
- [3] H.J. Dong, G. Chen, J.X. Sun, C.M. Li, Y.G. Yu, D.H. Chen, Appl. Catal., B: Environ. 134–135 (2013) 46–54.
- [4] H. Tong, S. Ouyang, Y. Bi, N. Umezawa, M. Oshikiri, J. Ye, Adv. Mater. 24 (2012) 229–251.
- [5] J.X. Sun, G. Chen, J.Z. Wu, H.J. Dong, G.H. Xiong, Appl. Catal., B: Environ. 132–133 (2013) 304–314.
- [6] Q.J. Xiang, J.G. Yu, M. Jaroniec, J. Am. Chem. Soc. 134 (2012) 6575–6578.
- [7] X. Li, X. Zhen, S. Meng, J. Xian, Y. Shao, X. Fu, D. Li, Environ. Sci. Technol. 47 (2013) 9911–9917.
- [8] X. Chen, S. Shen, L. Guo, S.S. Mao, Chem. Rev. 110 (2010) 6503–6570.
- [9] S.X. Ouyang, J.H. Ye, J. Am. Chem. Soc. 133 (2011) 7757–7763.
- [10] X. Pan, Y. Zhao, S. Liu, C.L. Korzeniewski, S. Wang, Z.Y. Fan, ACS Appl. Mater. Interfaces 4 (2012) 3944–3950.
- [11] X.Y. Pan, Y.J. Xu, J. Phys. Chem. C 117 (2013) 17996–18005.
- [12] R.D. Schaller, V.I. Klimov, Phys. Rev. Lett. 92 (2004) 186601.
- [13] M.A. Holmes, T.K. Townsend, F.E. Osterloh, Chem. Commun. 48 (2012) 371–373.
- [14] M. Liu, D. Jing, Z. Zhou, L. Guo, Nat. Commun. 4 (2013) 2278.
- [15] A. Stavrinadi, A.K. Rath, F.P.G. de Arquer, S.L. Diederhosen, C. Magén, L. Martinez, D. So, G. Konstantatos, Nat. Commun. 4 (2013) 2981.
- [16] L. Pan, J.J. Zou, S.B. Wang, Z.F. Huang, A. Yu, L. Wang, X.W. Zhang, Chem. Commun. 49 (2013) 6593–6595.
- [17] C.Y. Wang, H. Zhang, F. Li, L.Y. Zhu, Environ. Sci. Technol. 44 (2010) 6843–6848.
- [18] L.S. Zhang, W.Z. Wang, Z.G. Chen, L. Zhou, H.L. Xu, W. Zhu, J. Mater. Chem. 17 (2007) 2526–2532.
- [19] A.K.P. Mann, S.E. Skrabalak, Chem. Mater. 23 (2011) 1017–1022.
- [20] Y.L. Tian, B.B. Chang, J.L. Lu, J. Fu, F.N. Xi, X.P. Dong, ACS Appl. Mater. Interfaces 5 (2013) 7079–7085.
- [21] L.S. Zhang, W.Z. Wang, L. Zhou, H.L. Xu, Small 3 (2007) 1618–1625.
- [22] Z.J. Zhang, W.Z. Wang, E. Gao, S.M. Sun, L. Zhang, J. Phys. Chem. C 116 (2012) 25898–25903.
- [23] L.S. Zhang, K.H. Wong, Z.G. Chen, J.C. Yu, J.C. Zhao, C. Hu, C.Y. Chan, P.K. Wong, Appl. Catal., A: Gen. 363 (2009) 221–229.
- [24] H.G. Yu, R. Liu, X.F. Wang, P. Wang, J.G. Yu, Appl. Catal., B: Environ. 111–112 (2012) 326–333.
- [25] J.Y. Liu, Y. Bai, P.Q. Wang, Micro Nano Lett. 8 (2013) 90–93.
- [26] R.M. Mohamed, E.S. Aazam, Mater. Res. Bull. 48 (2013) 3572–3582.
- [27] F. Duan, Y. Zheng, M.Q. Chen, Appl. Surf. Sci. 257 (2011) 1972–1978.
- [28] L. Guo, D.J. Wang, F. Fu, X.D. Qiang, T. Xu, Adv. Mater. Res. 518–523 (2012) 833–836.
- [29] L. Ge, J. Liu, Appl. Catal., B: Environ. 105 (2011) 289–297.
- [30] J.Y. Ouyang, J.A. Ripmeester, X.H. Wu, D. Kingston, K. Yu, A.G. Joly, W. Chen, J. Phys. Chem. C 111 (2007) 16261–16266.
- [31] X.X. Xue, W. Ji, Z. Mao, H.J. Mao, Y. Wang, X. Wang, W.D. Ruan, B. Zhao, J.R. Lombardi, J. Phys. Chem. C 116 (2012) 8792–8797.
- [32] J.H. Byeon, Y.W. Kim, ACS Appl. Mater. Interfaces 5 (2013) 3959–3966.
- [33] R.H. Ouyang, J.X. Liu, W.X. Li, J. Am. Chem. Soc. 135 (2013) 1760–1771.
- [34] K. Yamaguchi, S. Inasawa, Y. Yamaguchi, J. Phys. Chem. C 116 (2012) 19978–19983.
- [35] M.A. Lovette, M.F. Doherty, Cryst. Growth Des. 12 (2012) 656–669.
- [36] A. Chernov, Sov. Phys. Crystallogr. 16 (1972) 734–753.
- [37] Z.Z. Lou, B.B. Huang, X.Y. Qin, X.Y. Zhang, H.F. Cheng, Y.Y. Liu, S.Y. Wang, J.P. Wang, Y. Dai, Chem. Commun. 48 (2012) 3488–3490.
- [38] M.S. Jin, H. Zhang, Z.X. Xie, Y.N. Xia, Angew. Chem. Int. Ed. 50 (2011) 7850–7854.
- [39] W.D. Shi, S. Yu, P. Liu, W.Q. Fan, CrystEngComm 15 (2013) 2978–2985.
- [40] S.F. Xie, H.C. Peng, N. Lu, J.G. Wang, M.J. Kim, Z.X. Xie, Y.N. Xia, J. Am. Chem. Soc. 135 (2013) 16658–16667.
- [41] W.H. Ni, X.S. Kou, Z. Yang, J.F. Wang, ACS Nano 2 (2008) 677–686.
- [42] Y.F. Li, Z.P. Liu, J. Am. Chem. Soc. 133 (2011) 15743–15752.
- [43] Y. Wu, K. Eisele, M. Doroshenko, G. Algara-Siller, U. Kaiser, K. Koynov, T. Weil, Small 8 (2012) 3465–3475.
- [44] Y.H. Chang, C.M. Liu, H.E. Cheng, C. Chen, ACS Appl. Mater. Interfaces 5 (2013) 3549–3555.
- [45] Y. Su, B.L. Zhu, K. Guan, S.S. Gao, L. Lv, C.F. Du, L.M. Peng, L.C. Hou, X.J. Wang, J. Phys. Chem. C 116 (2012) 18508–18517.
- [46] Y.H. Zheng, L.R. Zheng, Y.Y. Zhan, X.Y. Lin, Q. Zheng, K.M. Wei, Inorg. Chem. 46 (2007) 6980–6986.
- [47] S.K. Haram, A. Kshirsagar, Y.D. Gujarathi, P.P. Ingole, O.A. Nene, G.B. Markad, S.P. Nanavati, J. Phys. Chem. C 115 (2011) 6243–6249.
- [48] J. Zhao, M.A. Holmes, F.E. Osterloh, ACS Nano 7 (2013) 4316–4325.
- [49] A. Kudo, I. Tsuji, H. Kato, Chem. Commun. (2002) 1958–1959.
- [50] X.G. Luo, L.M. Liu, Z.P. Hu, W.H. Wang, W.X. Song, F.F. Li, S.J. Zhao, H. Liu, H.T. Wang, Y.J. Tian, J. Phys. Chem. Lett. 3 (2012) 3373–3378.
- [51] M. Sun, G.D. Chen, Y.K. Zhang, Q. Wei, Z.M. Ma, B. Du, Ind. Eng. Chem. Res. 51 (2012) 2897–2903.
- [52] I.K. Konstantinou, T.A. Albanis, Appl. Catal., B: Environ. 49 (2004) 1–14.
- [53] H.Z. Zhang, R.L. Zong, Y.F. Zhu, J. Phys. Chem. C 113 (2009) 4605–4611.
- [54] Y.H. Ng, I.V. Lightcap, K. Goodwin, M. Matsumura, P.V. Kamat, J. Phys. Chem. Lett. 1 (2010) 2222–2227.
- [55] Y.T. Liang, B.K. Vijayan, O. Lyandres, K.A. Gray, M.C. Hersam, J. Phys. Chem. Lett. 3 (2012) 1760–1765.
- [56] V. Etacheri, G. Michlits, M.K. Seery, S.J. Hinder, S.C. Pillai, ACS Appl. Mater. Interfaces 5 (2013) 1663–1672.
- [57] J.X. Yuan, Q. Wu, P. Zhang, J.H. Yao, T. He, Y.A. Cao, Environ. Sci. Technol. 46 (2012) 2330–2336.
- [58] D.J. Yang, H.W. Liu, Z.F. Zheng, Y. Yuan, J.C. Zhao, E.R. Wacławik, X.B. Ke, H.Y. Zhu, J. Am. Chem. Soc. 131 (2009) 17885–17893.
- [59] Y.M. Xu, C.H. Langfor, Langmuir 17 (2001) 897–902.